J. Fluid Mech. (2025), *vol*. 1003, A24, doi:10.1017/jfm.2024.1218

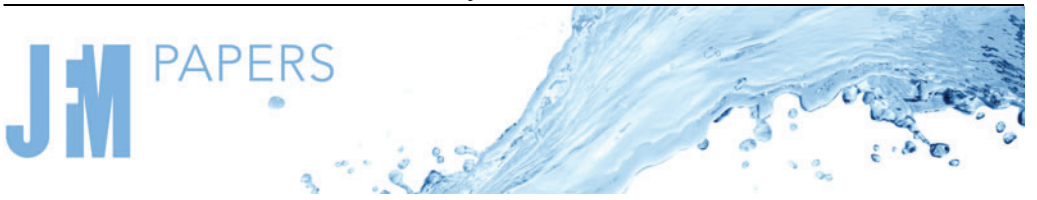

Active and inactive contributions to the wall pressure and wall-shear stress in turbulent boundary layers

Rahul Deshpande[1],†, **Ricardo Vinuesa**[2], **Joseph Klewicki**[1] **and Ivan Marusic**[1]

[1]Dept. Mechanical Eng., University of Melbourne, Parkville, VIC 3010, Australia

[2]FLOW, Eng. Mechanics, KTH Royal Institute of Technology, Stockholm 10044, Sweden

(Received 30 April 2024; revised 14 December 2024; accepted 15 December 2024)

A phenomenological description is presented to explain the intermediate and low-frequency/large-scale contributions to the wall-shear-stress (τ_w) and wall-pressure (p_w) spectra of canonical turbulent boundary layers, both of which are well known to increase with Reynolds number, albeit in a distinct manner. The explanation is based on the concept of active and inactive motions (Townsend, *J. Fluid Mech.*, vol. 11, issue 1, 1961, pp. 97–120) associated with the attached-eddy hypothesis. Unique data sets of simultaneously acquired τ_w, p_w and velocity-fluctuation time series in the log region are considered, across a friction-Reynolds-number (Re_τ) range of $O(10^3) \lesssim Re_\tau \lesssim O(10^6)$. A recently proposed energy-decomposition methodology (Deshpande *et al.*, *J. Fluid Mech.*, vol. 914, 2021, A5) is implemented to reveal the active and inactive contributions to the τ_w- and p_w-spectra. Empirical evidence is provided in support of Bradshaw's (*J. Fluid Mech.*, vol. 30, issue 2, 1967, pp. 241–258) hypothesis that the inactive motions are responsible for the non-local wall-ward transport of the large-scale inertia-dominated energy, which is produced in the log region by active motions. This explains the large-scale signatures in the τ_w-spectrum, which grow with Re_τ despite the statistically weak signature of large-scale turbulence production, in the near-wall region. For wall pressure, active and inactive motions respectively contribute to the intermediate and large scales of the p_w-spectrum. Both these contributions are found to increase with increasing Re_τ owing to the broadening and energization of the wall-scaled (attached) eddy hierarchy. This potentially explains the rapid Re_τ-growth of the p_w-spectra relative to τ_w, given the dependence of the latter only on the inactive contributions.

Key words: turbulent boundary layers, boundary layer structure

† Email address for correspondence: raadeshpande@gmail.com

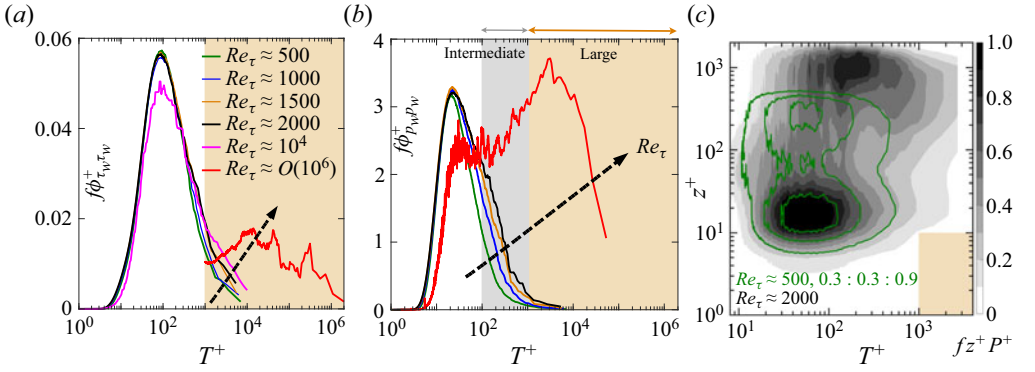

Figure 1. Premultiplied energy spectra of (*a*) τ_w, (*b*) p_w and (*c*) premultiplied spectrogram of the bulk turbulence production (fz^+P^+) as a function of $T^+(=1/f^+)$. Data for $500 \lesssim Re_\tau \lesssim 2000$ are from Eitel-Amor, Örlü & Schlatter (2014), for $Re_\tau \sim O(10^4)$ are from Marusic *et al.* (2021) and for $Re_\tau \sim O(10^6)$ are from the Surface Layer Turbulence and Environmental Science Test (SLTEST) facility data sets acquired by (*a*) Marusic & Heuer (2007) and (*b*) Klewicki, Priyadarshana & Metzger (2008). Grey and yellow coloured backgrounds in (*a–c*) indicate the nominal intermediate ($O(10^2) \lesssim T^+ \lesssim O(10^3)$) and large-scale ranges ($T^+ \gtrsim O(10^3)$), respectively.

1. Introduction and motivation

Wall-bounded flows are ubiquitous in various applications, such as over aircraft wings and around submarines, where they affect vessel performance through the imposition of wall-shear-stress (τ_w) and wall-pressure (p_w) fluctuations on the bounding surface. The former, τ_w, are associated with the skin-friction drag which limits vehicle speed, while the latter, p_w, are responsible for flow-induced vibrations that affect structural stability and generate noise. Nevertheless, accurately modelling the fluctuations in τ_w and p_w remains a challenge due to the limited understanding of the dependence of their generation mechanisms on the Reynolds number.

Figure 1 shows a compilation of premultiplied frequency spectra of τ_w and p_w for a wide range of Reynolds numbers. Here, the viscous-scaled time is defined as $T^+ = U_\tau^2/(f\nu)$, where f is the frequency of turbulence scales, ν is the kinematic viscosity and U_τ is the mean friction velocity, with superscript '+' indicating viscous scaling. All these spectra have been computed from previously published high-fidelity simulations ($500 \lesssim Re_\tau \lesssim 2000$) and experimental data sets ($O(10^4) \lesssim Re_\tau \lesssim O(10^6)$) of a turbulent boundary layer (TBL), where $Re_\tau = U_\tau\delta/\nu$ is the friction Reynolds number and δ is the TBL thickness. Although the experimental spectra have certain limitations at $T^+ \lesssim 100$ owing to spatial and temporal resolution, they will not influence this discussion (see § 3).

A noteworthy observation from figure 1(*a*,*b*) is the increasing energy contribution to the τ_w – ($T^+ \gtrsim O(10^3)$) and p_w-spectra ($T^+ > O(10^2)$) with increasing Re_τ, which has been noted previously in all canonical wall flows (Tsuji *et al.* 2007; Örlü & Schlatter 2011; Mathis *et al.* 2013; Panton, Lee & Moser 2017; Yu, Ceci & Pirozzoli 2022; Baars, Dacome & Lee 2024). While these viscous-scaled spectra exhibit Re_τ-invariance in the small-scale range ($T^+ \lesssim 100$), they exhibit distinct Re_τ-variations in the intermediate ($O(10^2) \lesssim T^+ \lesssim O(10^3)$) and large-scale ranges ($T^+ \gtrsim O(10^3)$), with these nominal bounds considered based on the largest possible Re_τ-range (figure 1*a*,*b*). Although past studies have broadly linked these Re_τ trends to the energization of large inertial motions, the present study addresses two fundamental questions that have remained unanswered: (i) Which motions are responsible for transporting the large-scale energy (i.e. energy of large-scale motions), residing in the outer region, towards the wall to influence the

wall-shear stress (Lee & Moser 2019; Lee & Hwang 2024)? (ii) Which motions contribute to the rapid Re_τ-growth of p_w in the intermediate scales ($O(10^2) \lesssim T^+ \lesssim O(10^3)$), and why is this growth relatively weaker in the case of τ_w?

The origin of the large-scale inertia-dominated energy in the outer region has now been well established in the literature (Lee & Moser 2019), based on the turbulent kinetic energy (TKE) production term, $P^+ = -2\overline{uw}^+(\partial U^+/\partial z^+)$. Here, u, v and w represent instantaneous velocity fluctuations along the streamwise (x), spanwise (y) and wall-normal (z) directions, respectively, while capital letters and overbar indicate time averaging. Figure 1(c) shows the premultiplied spectra of the bulk turbulence production ($fz^+P^+(z^+;T^+)$) from the same simulation data sets as in figure 1(a,b). Note here that the premultiplication with z^+ artificially amplifies the spectral content in the outer region compared with the inner region, but the majority of the energy production essentially occurs near the wall when $Re_\tau \lesssim O(10^3)$. Figure 1(c) confirms the weak energy production in the near-wall large scales ($T^+ > 1000$) compared with the small scales, thereby suggesting association of the large-scale τ_w-signatures with wall-ward energy transport from the outer region (Lee & Hwang 2024). While several past studies have quantified and predicted the superposition of large-scale signatures on τ_w (Metzger & Klewicki 2001; Örlü & Schlatter 2011; Mathis *et al.* 2013), fundamental understanding of their energy-transfer mechanisms is still lacking, starting from the motions governing the transport of large-scale energy from outer region towards the wall.

With regards to the differences between τ_w and p_w over $O(10^2) \lesssim T^+ \lesssim O(10^3)$, although considerable TKE is produced in this scale range in the inner region, the contour levels of the TKE production spectra in figure 1(c) exhibit a convincing collapse/invariance across different Re_τ. This suggests a negligible Re_τ-increment in the near-wall TKE production in the intermediate-scale range ($O(10^2) \lesssim T^+ \lesssim O(10^3)$), consistent with results presented by Lee & Moser (2019). It means that the Re_τ increase of $f\phi^+_{p_wp_w}$ in the intermediate-scale range is also associated with the energization of turbulence motions farther away from the wall, which, however, seem to influence $f\phi^+_{\tau_w\tau_w}$ relatively weakly. The present study attempts to advance our fundamental understanding of the turbulence motions governing these trends, and their roles in the underlying energy-transfer mechanisms. This information would be valuable for designing high$-Re_\tau$ drag and noise reduction strategies in the future.

2. Active and inactive components and their roles in the energy-transfer mechanisms

This study explores the ability of the attached-eddy (i.e. wall-scaled eddy; Townsend 1976) framework to provide a phenomenological explanation for the questions raised above. This is motivated by the fact that the same framework has been previously successful in predicting the τ_w- and p_w-spectra, associated with the inertial scales, across a broad Re_τ-range (Ahn, Graham & Rizzi 2010; Marusic *et al.* 2021). Per Townsend's hypothesis, the outer region ($z \gtrsim z_{min}$) of a high$-Re_\tau$ wall-bounded flow can be statistically represented by a hierarchy ($O(z_{min}) \lesssim \mathcal{H} \lesssim O(\delta)$) of geometrically self-similar, inviscid, wall-scaled eddies dominated by inertia (figure 2), where $\mathcal{H}$ is the eddy height and z_{min} is the nominal lower bound of the log region. These wall-scaled eddies have been classically referred to as attached eddies in the literature, in reference to their scaling with z and U_τ, and not necessarily implying their physical extension to the wall. Townsend (1976) proposed that these eddies have a population density varying inversely to their height $\mathcal{H}$, leading their cumulative velocity contributions at $z \gtrsim z_{min}$ to

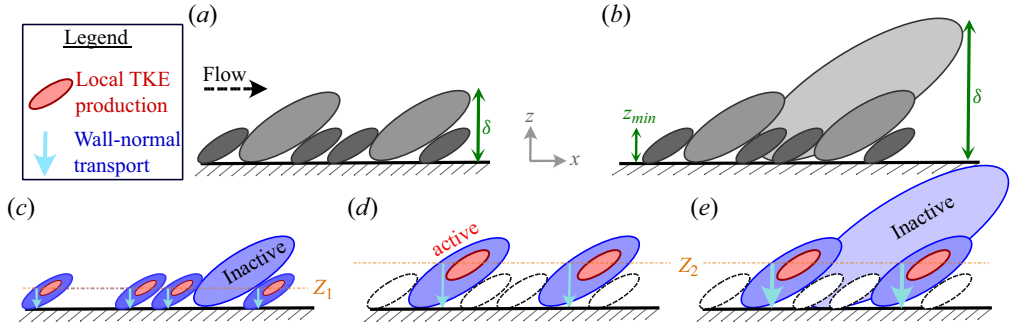

Figure 2. Conceptual sketches of wall-scaled eddies in a TBL at relatively (*a*) low (Re_{τ_1}) and (*b*) high (Re_{τ_2}) Reynolds numbers. (*c–e*) Depict the roles of the active and inactive parts of wall-scaled eddies in the energy-transfer mechanisms per the hypotheses of Bradshaw (1967) and de Giovanetti, Hwang & Choi (2016). Blue and red sections, respectively, correspond to the inactive and active portions of the wall-scaled eddies (grey scaled), which are defined based on the point of observation, z: (*c*) z_1 or (*d*,*e*) z_2. In (*d*,*e*), white eddies with dashed contours are centred lower than z, and hence are not involved in either local TKE production at z (red region), or non-local energy transport from z to the wall (cyan arrows). Greater thickness of the arrows in (*e*) indicates larger transport magnitude at higher Re_τ. Panels show (*a*) Re_{τ_1}; (*b*) $Re_{\tau_2} > Re_{\tau_1}$; (*c*) Re_{τ_1}, point of observation: z_1; (*d*) Re_{τ_1}, point of observation: z_2; (*e*) Re_{τ_2}, point of observation: z_2.

follow (at asymptotically high Re_τ)

$$\left.\begin{aligned} \overline{u^2}^+ &= B_1 - A_1 \ln(z/\delta), \\ \overline{v^2}^+ &= B_2 - A_2 \ln(z/\delta), \\ \overline{w^2}^+ &= B_3 \quad \text{and} \\ \overline{uw}^+ &= B_4, \end{aligned}\right\} \tag{2.1}$$

where B_{1-4} and A_{1-2} are constants. The increased availability of high-Re_τ data over the past two decades has provided considerable empirical support to these expressions (Jimenez & Hoyas 2008; Hultmark *et al.* 2012; Lee & Moser 2015; Orlandi, Bernardini & Pirozzoli 2015) in the nominal log region of the TBL (the exact definition of which may vary in the literature). The disagreement beyond the log region is owing to the statistical significance of the non-wall-scaled eddy-type motions coexisting in boundary layers, particularly in the boundary layer wake region (Marusic & Perry 1995).

While the expressions for $\overline{u^2}^+$ and $\overline{v^2}^+$ in (2.1) suggest their dependence on Re_τ, $\overline{w^2}^+$ and $\overline{uw}^+$ are postulated to be Re_τ-independent in the large Re_τ limit. Townsend (1976) explained this contradiction by proposing that the flow at any point of observation ($z \gtrsim z_{min}$) comprises two components of wall-scaled eddies (figure 2) – an 'active' component of the wall-scaled eddy that is responsible for local turbulent transfer and accounts for the instantaneous Reynolds shear stresses (uw) at z, and an 'inactive' component that does not contribute to uw at z. Here, the inactive component predominantly comes from wall-scaled eddies much taller than z, which contribute to uw (i.e. behave as active motions) at wall-normal locations larger than z. Hence, while the active component is solely responsible for the local TKE production, Townsend (1976) described inactive motions as non-local 'swirling motions' whose 'effect on that part of the layer between the point of observation and the wall is one of slow random variation of 'mean velocity' which cause corresponding variation of wall stress'. These statements were supported by Bradshaw (1967) and de Giovanetti *et al.* (2016), who hypothesized that the inactive parts

of the wall-scaled eddies are responsible for transporting large-scale energy produced in the outer layer (by active parts), to the wall. As per Bradshaw (1967), this process is necessary to maintain the near-wall energy balance and is sketched in figure 2(*c–e*).

Although the non-local wall-normal transport of large-scale energy has been previously observed through correlation/spectral analysis of the TKE budget equations (Cho, Hwang & Choi 2018; Lee & Moser 2019; Yin, Hwang & Vassilicos 2024), its connection with the inactive part of the wall-scaled eddies has never been definitively established, primarily due to the lack of a reliable flow-decomposition methodology. Along the same lines, while the association of p_w-signatures with intense uw events is well known (Gibeau & Ghaemi 2021; Baars *et al.* 2024), their distinct correlations with uw-contributing (active) and non-contributing (inactive) components has never been explicitly established. Recently, Deshpande, Monty & Marusic (2021) proposed a spectral linear stochastic estimation (SLSE)-based methodology that enables data-driven decomposition of the log-region flow into its corresponding active and inactive components. This provides an opportunity to establish the association of active/inactive components with τ_w and p_w, and thereby explain their Re_τ-variation based on the Re_τ growth of the wall-scaled eddy hierarchy (figure 2).

2.1. *Revisiting the concept of active and inactive motions*

Before proceeding with the new analysis, we briefly review the concept of active and inactive motions by means of a simplified mathematical description, which is inspired by Townsend's original ideas and adapted from our previous work (Deshpande, Monty & Marusic 2020; Deshpande *et al.* 2021). We consider the simplest model of a wall-bounded flow comprising wall-scaled eddies as the only eddying motions, which are represented by hairpin-type vortical structures. It is important to note here, however, that the concept of active and inactive motions does not depend on the shape of the vortical structures, but is rather associated with the spatial distribution of velocity signatures generated by these vortical structures, as depicted in figure 3(*a*) (estimated by simple Biot–Savart calculations). The inviscid nature of the wall-scaled eddy model permits slip at the wall (i.e. finite u and v), while $w = 0$ is enforced at $z = 0$ to remain consistent with wall impermeability. These differences in the boundary conditions result in spatially localized w-signatures (and consequently uw-signatures) at z from any wall-scaled eddy of $\mathcal{H} \sim O(z)$, while the u- and v-signatures extend across $0 \lesssim z < \mathcal{H}$ (i.e. non-local; refer to figure 3*a*). It is these characteristics that distinguish the active and inactive contributions in the velocity flow field, despite both of them originating from the same wall-scaled vortical structures.

Differences in the active/inactive contributions to the Reynolds stresses can be understood by invoking Townsend's (1976) eddy-intensity function I_{ij} (where $i, j = u, v$ or w), depicted schematically in figure 3(*b*) for the four non-zero combinations of i, j (refer to (2.1)). Here, I_{ij} is representative of the contribution from each eddy to the normal and Reynolds shear stresses as a function of z, and this is sketched for wall-scaled eddies of three different heights ($\mathcal{H}_1$–$\mathcal{H}_3$) in figure 3(*b*), as an example. Effects of increasing Re_τ can be accounted for by including taller eddies of height $\mathcal{H}_4 > \mathcal{H}_3$ and so on. The wall-normal distributions of I_{ij} are inspired by the individual velocity distributions in figure 3(*a*), and they are used to explain the cumulative contributions to the Reynolds stresses (from the three eddies) at three different probe locations in figure 3(*b*). For instance, when the probe is positioned at $z \sim \mathcal{H}_1$, all three eddies will contribute to $\overline{u^2}(z)$ and $\overline{v^2}(z)$, while the contribution to $\overline{w^2}(z)$ and $\overline{uw}(z)$ would come solely from the eddy of height $\mathcal{H}_1$. However, upon increasing the probe location to $z \sim \mathcal{H}_2$, contributions to the wall-parallel stresses

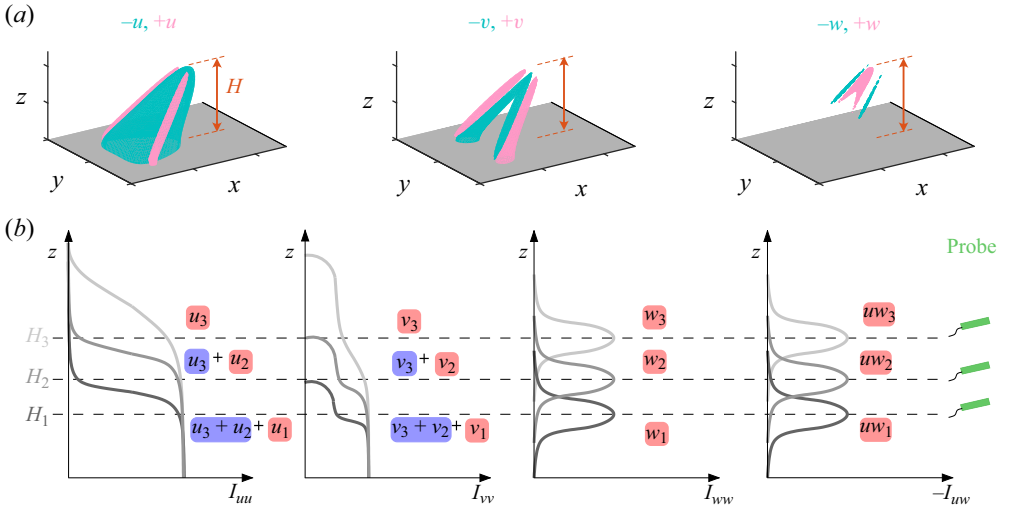

Figure 3. (*a*) Spatial signatures of the three velocity components (u, v, w) from a hairpin-type vortex structure of height $\mathcal{H}$, representative of a wall-scaled eddy (Marusic & Perry 1995). Regions in magenta and indigo, respectively, denote high- and low-momentum regions for the corresponding velocity fluctuations. (*b*) Eddy-intensity functions (I_{ij}) for wall-scaled eddies of three different heights $\mathcal{H}_i$, with $\mathcal{H}_1 < \mathcal{H}_2 < \mathcal{H}_3$. Here, u_i, v_i, w_i respectively denote velocity signatures generated from these wall-scaled eddies that are sensed by a probe, depending on their z-location. Red and blue background shadings of u_i, v_i, w_i, respectively, indicate active and inactive contributions at that location. The figure has been adapted from Deshpande *et al.* (2020).

are only made by the tallest two eddies, while those to $\overline{w^2}(z)$ and $\overline{uw}(z)$ only come from the eddy of height $\mathcal{H}_2$, and so on. Connecting these observations with Townsend's definitions in § 2, the active contributions at any z can be solely associated with eddies of height, $\mathcal{H} \sim O(z)$, which will contribute to u, v, w and hence uw, at z (indicated by red background shading in figure 3*b*). On the other hand, the inactive contributions are associated with relatively tall wall-scaled eddies: $O(z) \ll \mathcal{H} \lesssim O(\delta)$. These contribute to $u(z)$ and $v(z)$, but not $w(z)$ and $uw(z)$ (indicated by blue background shading).

Considering that increasing Re_τ introduces new eddies that are much taller than z, only the inactive contributions to $u(z)$ and $v(z)$ will increase for all $z \ll \mathcal{H}$, while the active contributions will exhibit Re_τ-invariance when scaled in wall units (i.e. z and U_τ). This explains the contrasting trends exhibited by the Reynolds stresses in (2.1), where $\overline{u^2}^+(z)$ and $\overline{v^2}^+(z)$ are Re_τ-dependent while $\overline{w^2}^+(z)$ and $\overline{uw}^+(z)$ exhibit Re_τ-invariance in the log region. In summary, both active and inactive motions contribute to the wall-parallel velocity fluctuations, but only the former contribute to the Reynolds shear stresses and w-fluctuations. This is expressed mathematically by the following (Panton 2007; Deshpande & Marusic 2021):

$$\left.\begin{aligned} u(z) &= u_a(z) + u_{ia}(z), \\ v(z) &= v_a(z) + v_{ia}(z) \quad \text{and} \\ w(z) &= w_a(z), \end{aligned}\right\} \tag{2.2}$$

where subscripts 'a' and 'ia', respectively, denote active and inactive components. The variances can be decomposed according to the following (Panton 2007; Deshpande &

Marusic 2021):

$$\left.\begin{aligned} \overline{u^2}^+ &= \overline{u_{ia}^2}^+ + \overline{u_a^2}^+ + 2\overline{u_{ia}u_a}, \\ \overline{v^2}^+ &= \overline{v_{ia}^2}^+ + \overline{v_a^2}^+ + 2\overline{v_{ia}v_a}, \\ \overline{w^2}^+ &= \overline{w_a^2}^+ \quad \text{and} \\ \overline{uw}^+ &= \overline{u_a w}^+ + \overline{u_{ia} w}^+. \end{aligned}\right\} \tag{2.3}$$

While $\overline{u_{ia}u_a}$, $\overline{v_{ia}v_a}$ and $\overline{u_{ia}w} = 0$ for a traditionally conceptualized wall-scaled eddy field (i.e. considering only linear superposition of velocity fluctuations originating from various hierarchies of wall-scaled eddies), that is not true for an actual/real wall-bounded flow (Deshpande *et al.* 2021; Deshpande & Marusic 2021). A real TBL also comprises very-large-scale inertial motions/superstructures that are inherently inactive per the definition of Townsend (Deshpande *et al.* 2021) and interact nonlinearly with/modulate the eddies local to z (Metzger & Klewicki 2001; Mathis *et al.* 2013; Baars, Hutchins & Marusic 2016). The causality between superstructures and nonlinear interactions, however, is a topic of ongoing debate (Andreolli *et al.* 2023). This, combined with the fact that these nonlinear interactions are smaller in magnitude than individual $\overline{u_{ia}^2}$ and $\overline{u_a^2}$ components (Deshpande & Marusic 2021), makes the investigation of nonlinear interactions beyond the scope of this study. The present study aims to deploy the decomposition methodology facilitating (2.2) on instantaneous flow fields of published data sets, to analyse for the first time the active and inactive contributions to τ_w and p_w. This work builds on the past successes of the decomposition methodology (Deshpande *et al.* 2021) that has yielded empirical support for the scaling characteristics of the active and inactive components, hypothesized by Townsend (1976). This includes the z-scaling behaviour of $\overline{u_a^2}^+$, and the inverse-logarithmic variation of $\overline{u_{ia}^2}^+$ associated with the k^{-1}-scaling (where k represents the streamwise/spanwise wavenumber), to list a few.

3. Data sets and methodology

The present study considers two previously published multi-point data sets across a large Re_τ range: $O(10^3) \lesssim Re_\tau \lesssim O(10^6)$, for the SLSE analysis. The low$-Re_\tau$ data set is from the high-resolution large-eddy simulation (LES) of a zero-pressure-gradient TBL by Eitel-Amor *et al.* (2014), which was computed over a numerical domain large enough for the TBL to evolve up to $Re_\tau \approx 2000$. In comparison with a fully resolved direct numerical simulation (DNS), the resolution employed in the LES data is just a factor of 2 coarser in the wall-parallel directions, and approximately 1.5 times coarser along the wall-normal one. Hence, instead of using a conventional subgrid-scale model in the simulation, a small forcing was implemented on the very small scales, essentially to add some extra dissipation. As a consequence, only two minor statistical differences emerge compared with a fully resolved DNS: a slight attenuation of the near-wall peak of $\overline{u^2}^+$, and a resolved TKE dissipation 87.2 % of that in a conventional DNS. However, adding the dissipation associated with the forcing recovers 99.8 % of the TKE dissipation. Since the present study predominantly focuses on the correlation between synchronously sampled time series of the desired wall properties (τ_w^+, p_w^+) and the overlying flow field (u^+, w^+), the use of a high-resolution LES instead of DNS does not influence the present conclusions. These correlations are investigated at designated streamwise locations of the numerical domain, corresponding to $Re_\tau \approx 500$, 1000, 1500 and 2000. For this, the time series of

the LES were sampled across the entire domain cross-section ($y-z$), with a resolution of $\Delta t^+ \lesssim 0.5$ and for a total eddy-turnover time ($t_{samp}U_\infty/\delta$) ≈ 243, where U_∞ is the free-stream speed. Combined with the option to ensemble average across the span, these time series are long enough to obtain a sufficiently converged frequency spectrum for capturing the inertial phenomena (demonstrated in Eitel-Amor *et al.* 2014).

The high-Re_τ ($\sim O(10^6)$) data set is from the neutrally buoyant surface layer at the SLTEST facility in Utah (Marusic & Heuer 2007). The data comprise synchronously acquired time series of (u^+, w^+) from five sonic anemometers positioned on a vertical tower, within the log region ($0.0025 < z/\delta < 0.0293$), and wall-shear-stress signals (τ_w^+) measured using a custom-designed sensor placed vertically below the sonics. These data were acquired at a time resolution of $\Delta t^+ \lesssim 78.4$ and for a total of 175 eddy-turnover times, across a viscous-scaled measuring volume of 1400 (of sonics).

While the sampling intervals for both LES and SLTEST data sets are not sufficient for fully converging/resolving the very-large-scale phenomena (quantitatively), they have been analysed previously by Deshpande, Vinuesa & Marusic (2024) and found to be sufficient to attain an accurate qualitative understanding. This was demonstrated by repeating the same statistical analysis (as presented ahead in § 3.1) on the simultaneous u^+, w^+ and τ_w^+ measurements conducted in the large Melbourne wind tunnel (Deshpande & Marusic 2021), time series for which were sampled for a much longer time interval and at greater frequency. The results and trends derived from the wind-tunnel data were qualitatively consistent with those obtained from the LES and SLTEST data sets, which will serve as the basis for the present study. Both these data sets provide rare access to velocity-fluctuation time series across the log region synchronously with τ_w, for TBLs spanning a broad Re_τ range (10^3–10^6). This offers a unique opportunity to directly test the hypotheses of Bradshaw (1967) and de Giovanetti *et al.* (2016), regarding TKE production and transport mechanisms from the log region to the wall, and to understand how they affect τ_w and p_w. Our present conclusions will only depend on the qualitative energy variation across z, and not focus on its quantification/scaling (requiring convergence). We note that, although the SLTEST flows are transitionally rough TBLs, the roughness effects are insignificant beyond the roughness sublayer (Klewicki *et al.* 2008; Marusic & Heuer 2007). Hence, the roughness will not influence the inertial eddies, which are our primary focus.

3.1. *Data-driven flow-decomposition methodology*

The multi-point nature of both the LES and SLTEST data sets permits theoretical estimation of u_a and u_{ia} by following the SLSE-based methodology proposed previously in Deshpande *et al.* (2021) and Deshpande & Marusic (2021). Throughout this paper, we limit our SLSE analysis to the log region where the concept of active and inactive motions, as well as expressions in (2.1), have received considerable empirical support (Deshpande *et al.* 2021). Per the SLSE methodology (Baars *et al.* 2016), the instantaneous component $u_{ia}(z)$ in the log region can be obtained by

$$\widetilde{u_{ia}}(z^+; T^+) = H_L(z^+; T^+)\widetilde{u_\tau}(T^+). \tag{3.1}$$

Here, $\widetilde{u_\tau}(T^+) = \sqrt{\widetilde{\tau_w/\rho}} = \mathcal{F}(u_\tau(t^+))$ is essentially the Fourier transform of the friction velocity fluctuations, $u_\tau(t^+)$, in time t, where ρ is density. The parameter $\widetilde{u_\tau}$ acts as the scale-specific unconditional input required to obtain the scale-specific conditional output, $\widetilde{u_{ia}}(z^+; T^+)$. The linear relationship between $\widetilde{u_{ia}}$ and $\widetilde{u_\tau}$ is inspired by the original definitions of active and inactive motions derived from the wall-scaled eddy model (refer § 2), which assumes a linear superposition of the velocity signatures generated by

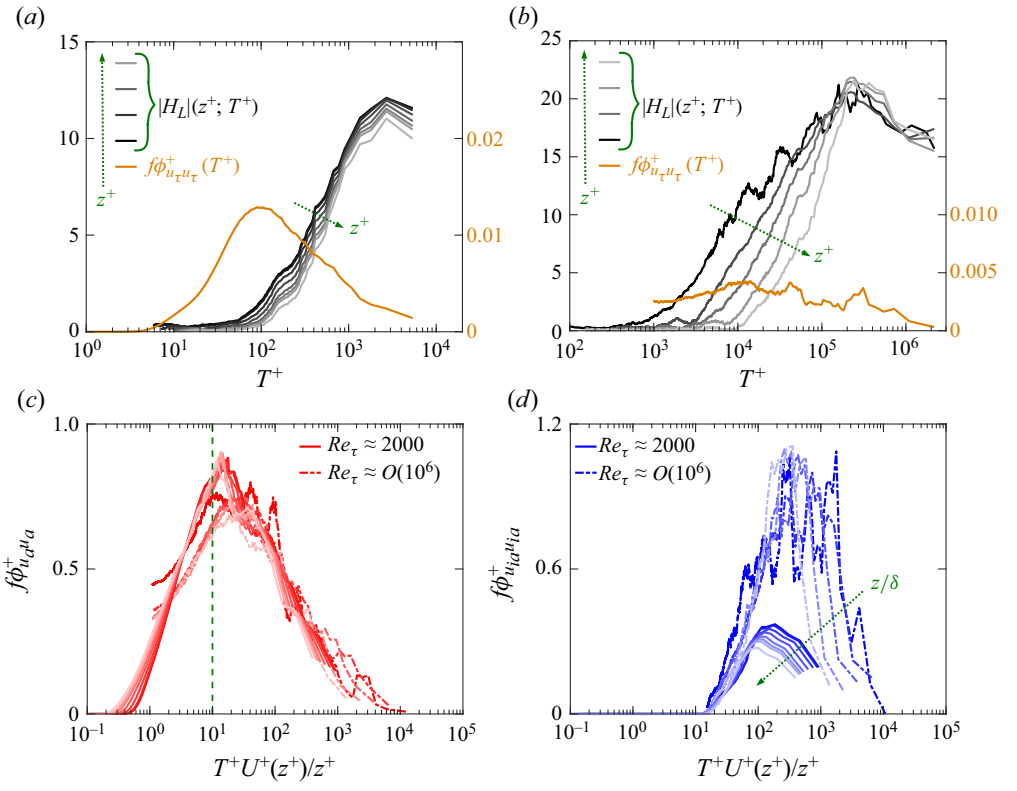

Figure 4. Absolute values of the linear transfer kernel ($|H_L|(z^+; T^+)$; (3.2)) computed for the (*a*) LES and (*b*) SLTEST data with grey shading representing changing z^+. Here, $|H_L|$ is plotted for z^+ limited to the log region and its ordinate is considered on the primary vertical axis (left; in black) while the solid golden line represents the premultiplied spectra of the friction velocity ($f\phi^+_{u_\tau u_\tau}$) and its ordinate is considered on the secondary vertical axis (right; in golden yellow). (*c*,*d*) Premultiplied spectra of the active (u_a) and inactive u-components (u_{ia}) estimated for various z-locations in the log region for both the LES and SLTEST data. Note that the horizontal axis is chosen to test for z-scaling of the spectra by invoking Taylor's hypothesis. Panels show data for (*a*) $Re_\tau \approx 2000$, (*b*) $Re_\tau \approx O(10^6)$, (*c*,*d*) both $Re_\tau \approx 2000$ and $Re_\tau \approx O(10^6)$.

individual eddies. Further, H_L is the complex-valued linear transfer kernel reconstructed by cross-correlating the synchronously acquired $\tilde{u}(z^+)$ and $\widetilde{u_\tau}$ according to the following:

$$H_L(z^+; T^+) = \frac{\{\tilde{u}(z^+; T^+)\widetilde{u_\tau}^*(T^+)\}}{\{\widetilde{u_\tau}(T^+)\widetilde{u_\tau}^*(T^+)\}}, \tag{3.2}$$

where the curly brackets ($\{\cdot\}$) and asterisk ($*$) denote ensemble averaging and complex conjugate, respectively. Here, the definition of H_L is underpinned by the discussion presented in § 2 and figure 3 that the inactive components coexisting at z^+ extend down to the wall (i.e. influence u_τ), while the active components are localized to z. Hence, (3.1) and (3.2) essentially classify $\widetilde{u_{ia}}$ as a subset of the total momentum $\tilde{u}$ that is coherent with $\widetilde{u_\tau}$. Figure 4(*a*,*b*) depicts $|H_L|(z^+, T^+)$ computed from the LES and SLTEST data sets at z^+ within the log region, alongside the premultiplied spectra of u_τ ($f\phi^+_{u_\tau u_\tau}$), where $|\cdot|$ represents the modulus. Before plotting, $|H_L|$ has been smoothed based on a 25 % bandwidth moving filter (Baars *et al.* 2016). This is done to remove the noise emerging from the mathematical operations in (3.2), which are conducted on a per-scale basis. It is evident that $|H_L|$ is non-zero across a broadband range of T^+ when z is close to the lower bound of the log region. However, $|H_L|$ gets restricted to relatively large scales

with an increase in z^+, essentially acting as a z-dependent low-pass filter conforming to larger scales with increasing z, in a manner consistent with Townsend's wall-scaled eddy hypothesis (refer § 2). These trends also align with the $|H_L|$ computed previously using long time-series signals from the Melbourne wind-tunnel data (Deshpande & Marusic 2021; Deshpande *et al.* 2024), confirming they are physical and not artefacts of insufficient convergence.

Significantly, for both the LES and SLTEST data, $|H_L|$ extends to sufficiently large T^+ values where the corresponding $f\phi^+_{u_\tau u_\tau}$ is negligible beyond the considered range. This ensures proper estimation of the very-large-scale $\widetilde{u_{ia}}$ signal. Similarly, the time resolution and frequency response of the wall-shear-stress sensor at high Re_τ, despite limiting the measurement of the wall-shear-stress spectrum to $T^+ \gtrsim 1000$ (figures 1*a* and 4*b*), is sufficient to resolve $\widetilde{u_{ia}}$ considering $|H_L| \sim 0$ at $T^+ \lesssim 1000$. The efficacy of extracting the inactive contributions is demonstrated by examining the scaling characteristics of the premultiplied u_{ia}-spectra ($f\phi^+_{u_{ia}u_{ia}}$; also see Deshpande *et al.* 2021). Figure 4(*d*) depicts $f\phi^+_{u_{ia}u_{ia}}$ estimated for various z/δ in the log region for the two data sets, and it is plotted against z-scaled streamwise wavelengths ($T^+U^+(z^+)/z^+$) computed based on Taylor's hypothesis (well accepted for inertial scales below 6δ; Dennis & Nickels 2008). Considering that inactive contributions at any z are associated with wall-scaled eddies across $O(z) \lesssim \mathcal{H} \lesssim O(\delta)$, $f\phi^+_{u_{ia}u_{ia}}$ is expected to exhibit z-scaling only in the relatively small-scale range, consistent with the trends in figure 4(*d*). Further, it is evident that the relatively large-scale contributions to $f\phi^+_{u_{ia}u_{ia}}$ decrease with z/δ across both data sets, which is also consistent with the inverse-logarithmic variation of $\overline{u_{ia}^2}$ expected based on the wall-scaled eddy hypothesis (refer to § 2 and Deshpande *et al.* 2021).

Once $\widetilde{u_{ia}}$ is obtained via (3.1), its time-domain equivalent can be calculated simply by taking the inverse Fourier transform (Deshpande & Marusic 2021) $u_{ia}(z^+; t^+) = \mathcal{F}^{-1}(\widetilde{u_{ia}}(z^+; T^+))$. Considering the discussion on the past hypotheses in § 2, the novel analysis here is not to establish the correlation of u_{ia} with τ_w (which is imposed by definition in (3.1)), but to investigate the variation of simultaneously acquired u_{ia}-signals across various z-locations in the log region (see § 4.1). Estimation of u_{ia} also permits calculation of the u_a-time series by simple subtraction, $u_a(z^+; t^+) = u(z^+; t^+) - u_{ia}(z^+; t^+)$, thereby associating u_a with the u-subset that is incoherent with the wall (i.e. u_τ). Similar to the investigation of $f\phi^+_{u_{ia}u_{ia}}$, we can examine the premultiplied u_a-spectrum ($f\phi^+_{u_au_a}$) for its expected scaling arguments. Per Townsend's (1976) hypothesis, active contributions at z are solely associated with wall-scaled eddies of $\mathcal{H} \sim O(z)$, suggesting $f\phi^+_{u_au_a}$ should exhibit z-scaling irrespective of the flow Re_τ. Figure 4(*c*) depicts reasonably good z-scaling of the premultiplied u_a-spectra across $O(10^3) \lesssim Re_\tau \lesssim O(10^6)$, consistent with the previous findings in Deshpande *et al.* (2021). This ability to estimate u_a enables computation of the Reynolds shear stresses associated exclusively with the active motions ($u_aw(z^+; t^+)$), which should correspond closely with the net Reynolds shear stresses ($uw(z^+; t^+)$) per Townsend's (1961) hypothesis. These hypotheses are tested in this study using simultaneously acquired time-series signals, across the log region, for the first time (see § 4.1).

4. Results and discussions

4.1. *Active and inactive contributions to the wall-shear stress*

This section focuses on responding to research question (i) raised in § 1, regarding the role played by inactive motions in transporting large-scale energy from the outer region

to the wall (to explain τ_w-signatures at large T^+). Figure 5(*a*,*f*) plots a small subset of the full u^+-time series sampled in the log region, synchronously with that of τ_w^+, from the LES and SLTEST data sets, respectively. These data are used to obtain the corresponding active (figure 5*c*,*h*) and inactive components (figure 5*e*,*j*) of u^+ by following the procedure described in § 3.1. As expected based on (3.1), u_{ia}-signals correspond predominantly to low-frequency features (i.e. large T^+) that are highly correlated with τ_w, while u_a-signals are representative of the intermediate-frequency phenomena that are uncorrelated with τ_w. This, however, should not be misinterpreted to imply negligible contributions of intermediate-scaled coherent structures to τ_w. Considering that the active–inactive classification is relative to z (refer § 2), subsets of the structures that are active at $z \sim z_1$ would be associated with inactive contributions much closer to the wall ($z \ll z_1$), and consequently influence τ_w from that location. Also plotted in figure 5(*b*,*g*) are the w^+-signals corresponding to the same instants as those considered for the u^+-signals. Notably, the w-signals exhibit the same characteristics as those of u_a across the log region. This is consistent with Townsend's description of u_a and w being associated with wall-scaled eddies local to z (i.e. $\mathcal{H} \sim z$), while u_{ia} corresponds to relatively taller and larger wall-scaled eddies ($O(z) \ll \mathcal{H} \lesssim O(\delta)$) whose contributions extend to the wall (refer § 2). It is worth noting here that active motions are deemed 'local' relative to their distance from the wall (i.e. $z \gg 0$). This should not be confused with the well-known localized behaviour of the Kolmogorov scales, which are spatially much smaller than the active–inactive motions (the latter being subsets of inertia-dominated motions). Hence, the active motions are bound to have a notable wall-normal coherence despite their 'localization', which is evident through the simultaneously acquired u_a- and w-signals across the log region in figure 5.

Townsend's (1976) hypothesis is mainly centred on the fact that the active components are solely responsible for the shear stresses and TKE production across the log region – this is clearly evident from figure 5(*d*,*i*) comparing $u_a w$ (in red) with uw (in thicker black lines). The good overlap of the two signals, across $10^3 \lesssim Re_\tau \lesssim 10^6$, is a testament to the capability of the SLSE-based methodology of extracting the active components from simultaneously acquired signals across the log region. The observations from figure 5(*i*) have been reaffirmed statistically in figure 6(*a*), where we compare the premultiplied co-spectra of the full Reynolds shear stress ($f\phi_{uw}^+$) with that associated solely with the active component ($f\phi_{u_a w}^+$), across various z/δ for the $Re_\tau \sim O(10^6)$ data set. The horizontal axis in this figure has been chosen to test for z-scaling of the co-spectra, by invoking Taylor's hypothesis (Dennis & Nickels 2008) similar to figure 4(*c*,*d*). In figure 6(*a*), $f\phi_{uw}^+$ and $f\phi_{u_a w}^+$ agree very well in the intermediate-scale range for all z/δ, with the co-spectrum peak exhibiting wall scaling at $T^+U^+(z^+) \approx 15z^+$. This reinforces the association of u_a with the active components per the definition of Townsend (1976).

There are, however, slight disagreements between $f\phi_{uw}^+$ and $f\phi_{u_a w}^+$ at the larger scales. This can be associated with the differences observed between the $u_a w$- and uw-time series in figure 5(*d*,*i*), at instants indicated by a green background. These are representative of the nonlinear interactions between the active motions and inactive superstructures (i.e. $u_{ia} w$), which become non-negligible only at time instants corresponding to high-amplitude signatures in u_{ia} (also highlighted by the green background in figure 5*e*,*j*). Notably, the magnitudes of these nonlinear interactions (i.e. $u_{ia} w$) are nominally of the same magnitude at $Re_\tau \approx 2000$ and $O(10^6)$, across various z/δ, which is consistent with the weak Re_τ-dependence of the inter-scale/nonlinear interactions reported by Mathis, Hutchins & Marusic (2009) across the log region. Hence, figure 6(*a*) reaffirms that the nonlinear

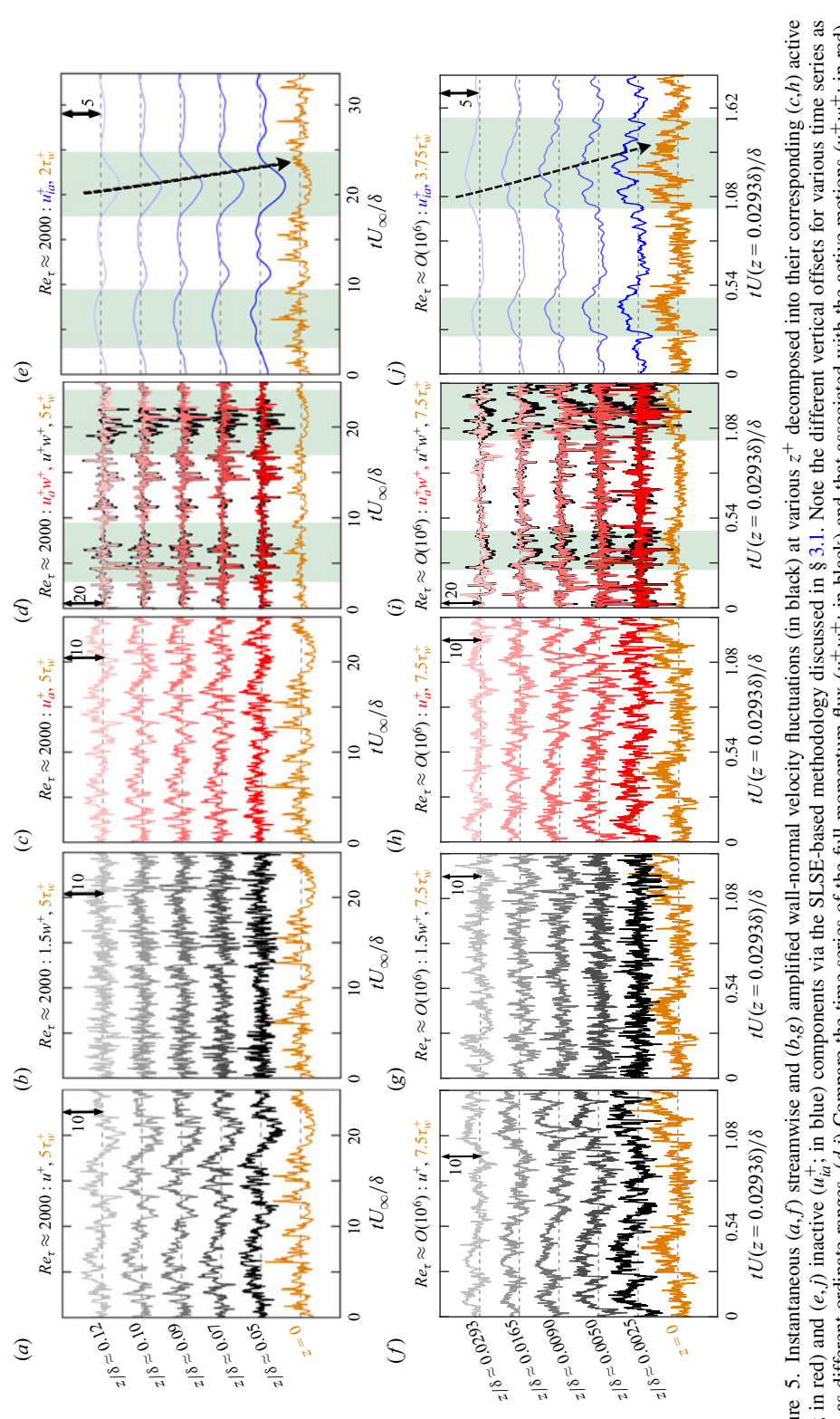

Figure 5. Instantaneous (*a*,*f*) streamwise and (*b*,*g*) amplified wall-normal velocity fluctuations (in black) at various z^+ decomposed into their corresponding (*c*,*h*) active (u_a^+; in red) and (*e*,*j*) inactive (u_{ia}^+; in blue) components via the SLSE-based methodology discussed in § 3.1. Note the different vertical offsets for various time series as well as different ordinate ranges. (*d*,*i*) Compare the time series of the full momentum flux (u^+w^+; in black) and that associated with the active motions ($u_a^+w^+$; in red). Dark to light shading indicates increase in z/δ across all plots. The synchronously acquired time series of the wall-shear-stress fluctuations (τ_w^+; in golden) have been plotted for: (*a*–*e*) $Re_\tau \approx 2000$ (LES) and (*f*–*j*) $Re_\tau \approx O(10^6)$ (SLTEST) data sets and has been intentionally amplified for clarity. Background green shading in (*d*,*e*,*i*,*j*) highlights portions of the time series associated with relatively high magnitudes of u_{ia}^+, which increase with decreasing z/δ indicating downward momentum transfer.

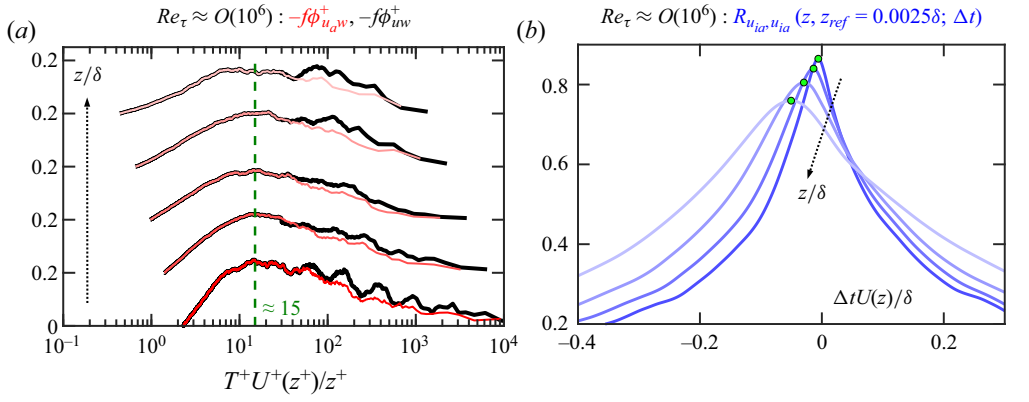

Figure 6. (*a*) Premultiplied co-spectra of the full Reynolds shear stress ($f\phi^+_{uw}$; in black) compared against those associated with the active component ($f\phi^+_{u_aw}$; in red) at various z/δ. Spectrum profiles for increasing z/δ are vertically offset by 0.2 for convenience of comparison. Dashed green line indicates z-scaling of the co-spectrum peak at $T^+U^+(z^+) \approx 15z$. (*b*) Cross-correlation between u_{ia} at $z_{ref} = 0.0025\delta$ and $z > z_{ref}$, with the maximum $R_{u_{ia}u_{ia}}$ highlighted by green circles.

interactions between the active and inactive components contribute towards a minor subset of the Reynolds shear stresses (and consequently, the $\overline{u^2}$ production), associated with the very large scales. These contributions, however, cannot be explained based on Townsend's wall-scaled eddy framework and is a shortcoming, requiring consideration in future upgrades of the model/framework.

Another notable observation from figure 5(*e*,*j*) is the discernible increase in u_{ia}-fluctuation magnitudes with decreasing z/δ, which can be compared based on the dashed grey lines representing zero magnitude (for signals at each z location). This suggests a wall-ward transport of streamwise momentum by the inactive components (indicated by the dashed black arrows) that is locally produced at each z by the active component (conceptualized in figure 2*c*–*e*). Since the correlation between u_{ia} and τ_w has already been quantified by $|H_L|$ via (3.2), we know that this transport occurs all the way down to the wall. The novel result here is the time-synchronized increment in u_{ia} magnitude with decreasing z, which is revealed only after the flow decomposition. It presents direct evidence of the non-local transfer of momentum/energy in the wall-normal direction across a broad Re_τ-range, which was previously noted only via spectral distributions at low Re_τ (Cho *et al.* 2018; Lee & Moser 2019). The average time delay/offset for the increase in u_{ia} magnitude, with decreasing z, can be estimated by computing the two-point correlation ($R_{u_{ia}u_{ia}}$) defined as follows:

$$R_{u_{ia}u_{ia}}(z, z_{ref}; \Delta t) = \frac{\overline{u_{ia}(z_{ref} \approx 0.0025\delta, t)u_{ia}(z, t + \Delta t)}}{\sqrt{\overline{u^2_{ia}(z_{ref} \approx 0.0025\delta)}}\sqrt{\overline{u^2_{ia}(z)}}}. \tag{4.1}$$

Figure 6(*b*) depicts $R_{u_{ia}u_{ia}}$ for the $Re_\tau \sim O(10^6)$ data at various $z > z_{ref}$. It is evident that the maxima of $R_{u_{ia}u_{ia}}$, which are highlighted by green circles, are found for a non-zero $|\Delta t|$ that increases with increasing z/δ. This can be interpreted as the average increase in time needed for the wall-normal energy transport, from z to z_{ref}.

The significance of this empirical evidence is highlighted by quoting text directly from de Giovanetti *et al.* (2016), who hypothesized that: 'the energy-containing motions, which essentially reside in the logarithmic and outer regions, transport the streamwise

momentum to the near-wall region through their inactive part, while generating Reynolds shear stress with their wall-detached wall-normal velocity component in the region much further from the wall'. Here, de Giovanetti *et al.* (2016) use 'wall detached' to essentially refer to the active component responsible for the w-fluctuations, given that it does not physically extend down to the wall. Hence, figure 5(*d*,*e*,*i*,*j*) cumulatively provides strong empirical evidence in support of the hypotheses proposed by Bradshaw (1967) and de Giovanetti *et al.* (2016). They also align with the recent conjecture by Lee & Hwang (2024), regarding the 'origin' of the large-scale τ_w-signatures based on outer energy transported to the wall.

Unfortunately, the data considered in this study do not permit a direct comparison of $\overline{u_{ia}^2}$ with $\overline{\tau_w^2}$ for increasing Re_τ, owing to mismatched z^+ and z/δ for the two data sets, alongside the under-resolved measurement of τ_w (both spatially and temporally). Interested readers may refer to discussions and analyses presented in Deshpande *et al.* (2021), wherein it is suggested that $\overline{u_{ia}^2}$ at a fixed z/δ would be expected to increase with Re_τ due to the broadening of the wall-scaled eddy hierarchy (see also figures 2*b*,*e* and 3). This insight potentially explains the Reynolds-number dependency of the low-frequency/large-scale signatures in the τ_w-spectra ($T^+ > 1000$), as noted in figure 1(*a*) and discussed in the literature (Örlü & Schlatter 2011; Mathis *et al.* 2013). These large-scale contributions, however, only correspond to a subset of the total inertial velocity signatures, i.e. the ones that are physically coherent with the wall. This, combined with the statistically dominant contribution from the near-wall streaks ($T^+ \lesssim O(10^3)$) is likely responsible for the weak Re_τ-growth of the τ_w-spectra in the intermediate scales ($O(10^2) \lesssim T^+ \lesssim O(10^3)$).

Besides testing past hypotheses, analysis in this section also demonstrates the unique capability to segregate instantaneous flow components associated with two key energy-transfer mechanisms in high Re_τ wall flows – TKE production and its wall-normal transport. This is a promising development for design of real-time control strategies targeting either of these mechanisms. However, more work is required with respect to identifying three-dimensional flow features/motions responsible for these mechanisms before such strategies can be actualized. As is evident from figure 5(*b*,*g*), the wall-normal transport cannot be explained purely based on the w-time series sampled across limited (and large) wall-normal offsets. But it could be possible by analysing velocity fluctuations/gradients acquired with good wall-normal resolution. This, however, is beyond the scope of the present study.

4.2. *Active and inactive contributions to the wall pressure*

This section focuses on addressing research question (ii) raised in § 1, regarding the inertial motions responsible for the Re_τ-growth of the p_w-spectra. For this, we compute the linear coherence spectrum (Gibeau & Ghaemi 2021; Baars *et al.* 2024) between the fluctuating wall-pressure and velocity fluctuations according to the following:

$$\gamma^2_{u_i p_w}(z^+; T^+) = \frac{|\{\widetilde{u_i}(z^+; T^+)\widetilde{p_w}^*(T^+)\}|^2}{\{\widetilde{u_i}(z^+; T^+)\widetilde{u_i}^*(z^+; T^+)\}\{\widetilde{p_w}(T^+)\widetilde{p_w}^*(T^+)\}}, \tag{4.2}$$

where u_i can be either u, w, u_{ia} or u_a, $(|\cdot|)$ represents absolute values, while all other notations are the same as in (3.2). Note that $\gamma^2_{u_i p_w}$ can be interpreted as the spectral equivalent of a physical two-point correlation between p_w and u_i, which varies in the range $0 \leq \gamma^2_{u_i p_w} \leq 1$ by definition. Furthermore, $\gamma^2_{up_w}$ and $\gamma^2_{wp_w}$ have been analysed previously for a canonical TBL at $Re_\tau \approx 2000$ by Gibeau & Ghaemi (2021), to establish the

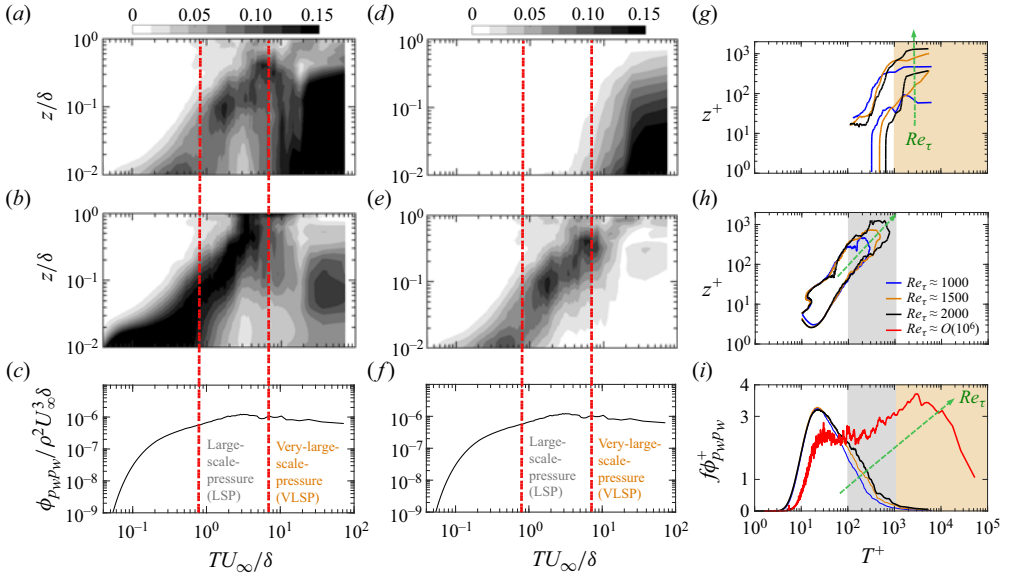

Figure 7. Linear coherence spectrum ($\gamma^2_{u_ip_w}$; (4.2)) computed between $u_i(z^+)$ and p_w as a function of outer- or inner-scaled T: (*a*) $\gamma^2_{up_w}$, (*b*) $\gamma^2_{wp_w}$, (*d*,*g*) $\gamma^2_{u_iap_w}$ and (*e*,*h*) $\gamma^2_{u_ap_w}$. (*a*,*b*,*d*,*e*) Depict $\gamma^2_{u_ip_w}$ computed from $Re_\tau \approx 2000$ LES data compared against the (*c*,*f*) outer-scaled p_w-spectrum plotted vs outer-scaled T. Panels (*g*,*h*), respectively, depict $\gamma^2_{u_iap_w}$ and $\gamma^2_{u_ap_w}$ contours for data across various Re_τ, which are compared against (i) $f\phi^+_{p_wp_w}$ plotted vs T^+. Panels show (*a*) $\gamma^2_{up_w}$, (*b*) $\gamma^2_{wp_w}$, (*d*) $\gamma^2_{u_iap_w}$, (*e*) $\gamma^2_{u_ap_w}$, (*g*) $\gamma^2_{u_iap_w} = 0.02, 0.09$, (*h*) $\gamma^2_{u_ap_w} = 0.07$.

scale-based coupling between the inertial motions and the large-scale pressure (LSP; $0.8 < TU_\infty/\delta < 7$), as well as the very-large-scale pressure (VLSP; $TU_\infty/\delta > 7$) regions of the p_w-spectrum. To validate our analysis, we recompute $\gamma^2_{up_w}$ and $\gamma^2_{wp_w}$ (figure 7*a*,*b*) from the LES data set at $Re_\tau \approx 2000$ and compare it with the outer-scaled p_w-spectrum (figure 7*c*). The coherence spectrum depicts characteristics consistent with those reported by Gibeau & Ghaemi (2021): the VLSP region is associated with relatively strong coherence between u and p_w, but not between w and p_w. While, in case of LSP, reasonable coherence can be noted between both u and p_w and w and p_w. If the same spectrograms were plotted as a function of streamwise wavelengths based on Taylor's hypothesis (i.e. $\lambda_x^+ = T^+U^+(z^+)$), the energetic ridges of $\gamma^2_{up_w}$ and $\gamma^2_{wp_w}$ would respectively exhibit distance-from-the-wall scalings: $\lambda_x/z = 14$ and $\lambda_x/z = 8.5$ (not shown here), consistent with Baars *et al.* (2024). Exhibition of this scaling confirms the association of the p_w-spectrum with the wall-scaled eddy hierarchy coexisting in the inertial/large-scale range.

Connecting the differences between $\gamma^2_{up_w}$ and $\gamma^2_{wp_w}$ with the characteristics of active and inactive components discussed in § 2, it can be hypothesized that the p_w-spectrum in the LSP and VLSP ranges, is, respectively, correlated to the active and inactive motions. The availability of decomposed u_a and u_{ia} components, for the same data as in figure 7(*a*,*b*), permits us to directly test this hypothesis by analysing the $\gamma^2_{u_iap_w}$ and $\gamma^2_{u_ap_w}$ results of figure 7(*d*,*e*), respectively. It is evident that the coherence between u_{ia} and p_w is limited to the VLSP range, while that between u_a and p_w (in the inertial region) is predominantly in the LSP range, similar to $\gamma^2_{wp_w}$. All the observations are consistent with our hypothesis above, with the similarity between $\gamma^2_{wp_w}$ and $\gamma^2_{u_ap_w}$ expected,

considering that w-signatures are predominantly from active contributions (see (2.2)). The present results offer phenomenological explanations for the conclusions drawn by Gibeau & Ghaemi (2021), who associated p_w-fluctuations in the LSP range with Reynolds shear-stress-carrying ejection and sweep events in the log region, i.e. the active components of the wall-scaled eddies. Conversely, p_w-fluctuations in the VLSP range were linked with the large δ-scaled motions and superstructures, which correspond to the inactive components transporting energy from the outer region to the wall. The results also confirm the dependency of p_w on velocity signatures that are coherent (akin to u_{ia}, amongst others) as well as incoherent (akin to u_a, amongst others) with the wall, consistent with the pressure Poisson equation (Tsuji *et al.* 2007).

Since the wall-scaled eddy hierarchy grows by coexisting in a physically taller log region with increasing Re_τ (figure 2*b*,*e*; Deshpande *et al.* 2021), the association of the LSP and VLSP ranges, with u_a and u_{ia}, can be used to explain the Re_τ-variation of the p_w-spectrum. To this end, figure 7(*g*,*h*) plots the constant energy contours of $\gamma^2_{u_{ia}p_w}$ and $\gamma^2_{u_ap_w}$ vs T^+ for $1000 \lesssim Re_\tau \lesssim 2000$, each of which exhibit their unique Re_τ-trends. Notably, the contours of $\gamma^2_{u_ap_w}$ can be seen to grow and widen across a larger T^+ range with Re_τ (indicated by green arrows), which explains the Re_τ-growth of the p_w-spectrum in the intermediate-scale range: $O(10^2) \lesssim T^+ \lesssim O(10^3)$. It suggests that a physically taller log region comprises a broader hierarchy of TKE-producing active motions, which subsequently increases contributions to the p_w-spectrum. This is analogous to the broadening of the $\overline{uw}$-plateau (~ -1) in the log region with increasing Re_τ ((2.1), Marusic & Perry 1995; Baidya *et al.* 2017). In contrast, the active motions do not contribute to the τ_w-spectrum since they do not physically extend down to the wall, and consequently do not influence the near-wall velocity gradient (de Giovanetti *et al.* 2016). It is thus obvious that the Re_τ trend of $f\phi^+_{p_wp_w}$ is governed by a broader range of inertial motions than those influencing $f\phi^+_{\tau_w\tau_w}$, likely explaining the stronger Re_τ-growth of the former compared with the latter. Note that arriving at this realization was made possible by decomposing the u–p_w coherence into its active and inactive components.

Similar to the behaviour of $\gamma^2_{u_ap_w}$, the contours of $\gamma^2_{u_{ia}p_w}$ can also be seen extending across a larger z^+-range with Re_τ. This is predominantly associated with the energization and increasing wall-normal extent of the large wall-scaled eddies and superstructures (Mathis *et al.* 2013; Lee & Moser 2019). At very high $Re_\tau \sim O(10^6)$, these energetic superstructures along with a broad hierarchy of wall-scaled eddies (figure 2*e*) contribute to the significantly enhanced VLSP signatures of the p_w-spectrum through their inactive component (figure 7*i*). The present analysis, hence, encourages future detailed multi-point measurements and high-fidelity simulations that can quantify the pressure–velocity coupling at high-Re_τ ($\gtrsim 10^4$), with particular focus on velocity signatures superimposed by the inertia-dominated motions. Consequently, it also motivates high-Re_τ investigations of the nonlinear interactions between the large-scale velocity signatures and p_w (Thomas & Bull 1983; Tsuji, Marusic & Johansson 2015), which have previously been limited to $Re_\tau \lesssim O(10^3)$.

5. Concluding remarks

This study clarifies the Re_τ-dependent, intermediate- and large-scale contributions to the τ_w- and p_w-spectra by invoking the attached (wall-scaled) eddy framework (Townsend 1976), based on active and inactive motions. Unique multi-point data sets are analysed using an energy-decomposition methodology to reveal the contributions from TKE-producing (active) and non-producing (inactive) components, at any wall-normal

position in the log region, to the τ_w- and p_w-spectra. Inactive components of wall-scaled eddies are found to be responsible for the non-local wall-normal transport of the large-scale inertia-dominated energy, from its origin in the log region (i.e. produced by active components) to the wall. On the other hand, the majority of the TKE-producing (i.e. active) motions in the log region are localized and physically detached from the wall, not influencing τ_w. These results provide strong empirical evidence for the hypotheses proposed by Bradshaw (1967) and de Giovanetti *et al.* (2016). They also explain the appearance and Re_τ-growth of the large-scale signatures in the τ_w-spectra, despite the insignificant large-scale TKE production occurring in the near-wall region. In terms of their contribution to wall pressure, the active and inactive components are respectively correlated with the intermediate- and large-scale portions of the p_w-spectrum. Both components exhibit growth with increasing Re_τ, which is attributed to the broadening of the wall-scaled eddy hierarchy. This is plausibly responsible for the rapid Re_τ-growth of the p_w-spectra relative to τ_w (figure 1*a*,*b*). These phenomenological explanations carry potential to influence future real-time control strategies, aimed at achieving energy-efficient drag and flow-noise reduction.

While this study demonstrates the new found capability to extract the instantaneous active and inactive components, also shedding light on their role in the large-scale energy-transfer mechanisms, it does not delve into the nonlinear/inter-scale interactions between these motions. These interactions, which have been previously discussed in the literature to a certain extent (Cho *et al.* 2018; Lee & Moser 2019), can likely explain the transfer of TKE produced by active components to the inactive component of the wall-scaled eddies, before being transported downward to the wall (figure 2). At this stage, these interactions are not accounted for within Townsend's wall-scaled eddy framework, which is inherently limited to the linear superposition of velocity signatures induced by the eddy structures. It does, however, highlight the opportunity for future upgrades/modifications to the model by incorporating the inter-scale interactions between the wall-scaled eddy hierarchy.

Funding. R.D. is supported by the University of Melbourne's Postdoctoral Fellowship and acknowledges insightful discussions with Drs W.J. Baars, B. Gibeau and S. Ghaemi. Funding is gratefully acknowledged from the Office of Naval Research: N62909-23-1-2068 (R.D., I.M.), and to R.V. from the European Research Council grant no. '2021-CoG-101043998, DEEPCONTROL'. Views/opinions expressed are, however, those of the author(s) only and do not necessarily reflect those of the European Union or the European Research Council. Neither the European Union nor the granting authority can be held responsible for them.

Declaration of interests. The authors report no conflict of interest.

Author ORCIDs.
Rahul Deshpande https://orcid.org/0000-0003-2777-2919;
Ricardo Vinuesa https://orcid.org/0000-0001-6570-5499;
Joseph Klewicki https://orcid.org/0000-0002-4921-3272;
Ivan Marusic https://orcid.org/0000-0003-2700-8435.

References

Ahn, B.-K., Graham, W.R. & Rizzi, S.A. 2010 A structure-based model for turbulent-boundary-layer wall pressures. *J. Fluid Mech.* **650**, 443–478.

Andreolli, A., Gatti, D., Vinuesa, R., Örlü, R. & Schlatter, P. 2023 Separating large-scale superposition and modulation in turbulent channels. *J. Fluid Mech.* **958**, A37.

Baars, W.J., Dacome, G. & Lee, M. 2024 Reynolds-number scaling of wall-pressure–velocity correlations in wall-bounded turbulence. *J. Fluid Mech.* **981**, A15.

BAARS, W.J., HUTCHINS, N. & MARUSIC, I. 2016 Spectral stochastic estimation of high-Reynolds-number wall-bounded turbulence for a refined inner-outer interaction model. *Phys. Rev. Fluids* **1** (5), 054406.

BAIDYA, R., PHILIP, J., HUTCHINS, N., MONTY, J.P. & MARUSIC, I. 2017 Distance-from-the-wall scaling of turbulent motions in wall-bounded flows. *Phys. Fluids* **29** (2), 020712.

BRADSHAW, P. 1967 'Inactive' motion and pressure fluctuations in turbulent boundary layers. *J. Fluid Mech.* **30** (2), 241–258.

CHO, M., HWANG, Y. & CHOI, H. 2018 Scale interactions and spectral energy transfer in turbulent channel flow. *J. Fluid Mech.* **854**, 474–504.

DENNIS, D.J.C. & NICKELS, T.B. 2008 On the limitations of Taylor's hypothesis in constructing long structures in a turbulent boundary layer. *J. Fluid Mech.* **614**, 197–206.

DESHPANDE, R. & MARUSIC, I. 2021 Characterising momentum flux events in high Reynolds number turbulent boundary layers. *Fluids* **6** (4), 168.

DESHPANDE, R., MONTY, J.P. & MARUSIC, I. 2020 Active and inactive motions in wall turbulence. In *Proceedings of 22nd Australasian Fluid Mechanics Conference* (ed. H. Chanson & R. Brown). The University of Queensland.

DESHPANDE, R., MONTY, J.P. & MARUSIC, I. 2021 Active and inactive components of the streamwise velocity in wall-bounded turbulence. *J. Fluid Mech.* **914**, A5.

DESHPANDE, R., VINUESA, R. & MARUSIC, I. 2024 Characteristics of active and inactive motions in high-Reynolds-number turbulent boundary layers. In *Proc. 13th Turbulence and Shear Flow Phenomenon (TSFP13), Montréal.*, arXiv:2404.18506 [physics.flu-dyn]. Begell House.

EITEL-AMOR, G., ÖRLÜ, R. & SCHLATTER, P. 2014 Simulation and validation of a spatially evolving turbulent boundary layer up to $Re_\theta = 8300$. *Intl J. Heat Fluid Flow* **47**, 57–69.

GIBEAU, B. & GHAEMI, S. 2021 Low-and mid-frequency wall-pressure sources in a turbulent boundary layer. *J. Fluid Mech.* **918**, A18.

DE GIOVANETTI, M., HWANG, Y. & CHOI, H. 2016 Skin-friction generation by attached eddies in turbulent channel flow. *J. Fluid Mech.* **808**, 511–538.

HULTMARK, M., VALLIKIVI, M., BAILEY, S.C.C. & SMITS, A.J. 2012 Turbulent pipe flow at extreme Reynolds numbers. *Phys. Rev. Lett.* **108** (9), 094501.

JIMENEZ, J. & HOYAS, S. 2008 Turbulent fluctuations above the buffer layer of wall-bounded flows. *J. Fluid Mech.* **611**, 215–236.

KLEWICKI, J.C., PRIYADARSHANA, P.J.A. & METZGER, M.M. 2008 Statistical structure of the fluctuating wall pressure and its in-plane gradients at high Reynolds number. *J. Fluid Mech.* **609**, 195–220.

LEE, M. & HWANG, Y. 2024 The origin of wall-shear stress fluctuations in wall-bounded turbulence. arXiv:2405.00591 [physics.flu-dyn].

LEE, M. & MOSER, R.D. 2015 Direct numerical simulation of turbulent channel flow up to $Re_\tau \approx 5200$. *J. Fluid Mech.* **774**, 395–415.

LEE, M. & MOSER, R.D. 2019 Spectral analysis of the budget equation in turbulent channel flows at high Reynolds number. *J. Fluid Mech.* **860**, 886–938.

MARUSIC, I., CHANDRAN, D., ROUHI, A., FU, M.K., WINE, D., HOLLOWAY, B., CHUNG, D. & SMITS, A.J. 2021 An energy-efficient pathway to turbulent drag reduction. *Nat. Commun.* **12** (1), 1–8.

MARUSIC, I. & HEUER, W.D.C. 2007 Reynolds number invariance of the structure inclination angle in wall turbulence. *Phys. Rev. Lett.* **99** (11), 114504.

MARUSIC, I. & PERRY, A.E. 1995 A wall-wake model for the turbulence structure of boundary layers. Part 2. Further experimental support. *J. Fluid Mech.* **298**, 389–407.

MATHIS, R., HUTCHINS, N. & MARUSIC, I. 2009 Large-scale amplitude modulation of the small-scale structures in turbulent boundary layers. *J. Fluid Mech.* **628**, 311–337.

MATHIS, R., MARUSIC, I., CHERNYSHENKO, S.I. & HUTCHINS, N. 2013 Estimating wall-shear-stress fluctuations given an outer region input. *J. Fluid Mech.* **715**, 163–180.

METZGER, M.M. & KLEWICKI, J.C. 2001 A comparative study of near-wall turbulence in high and low Reynolds number boundary layers. *Phys. Fluids* **13** (3), 692–701.

ORLANDI, P., BERNARDINI, M. & PIROZZOLI, S. 2015 Poiseuille and Couette flows in the transitional and fully turbulent regime. *J. Fluid Mech.* **770**, 424–441.

ÖRLÜ, R. & SCHLATTER, P. 2011 On the fluctuating wall-shear stress in zero pressure-gradient turbulent boundary layer flows. *Phys. Fluids* **23** (2), 021704.

PANTON, R.L. 2007 Composite asymptotic expansions and scaling wall turbulence. *Phil. Trans. R. Soc.* A **365** (1852), 733–754.

PANTON, R.L., LEE, M. & MOSER, R.D. 2017 Correlation of pressure fluctuations in turbulent wall layers. *Phys. Rev. Fluids* **2** (9), 094604.

THOMAS, A.S. & BULL, M.K. 1983 On the role of wall-pressure fluctuations in deterministic motions in the turbulent boundary layer. *J. Fluid Mech.* **128**, 283–322.

TOWNSEND, A.A. 1961 Equilibrium layers and wall turbulence. *J. Fluid Mech.* **11** (1), 97–120.

TOWNSEND, A.A. 1976 *The Structure of Turbulent Shear Flow*, 2nd edn. Cambridge University Press.

TSUJI, Y., FRANSSON, J., ALFREDSSON, P. & JOHANSSON, A. 2007 Pressure statistics and their scaling in high-Reynolds-number turbulent boundary layers. *J. Fluid Mech.* **585**, 1–40.

TSUJI, Y., MARUSIC, I. & JOHANSSON, A.V. 2015 Amplitude modulation of pressure in turbulent boundary layer. *Intl J. Heat Fluid Flow* **61**, 2–11.

YIN, L., HWANG, Y. & VASSILICOS, J.C. 2024 Dynamics of turbulent energy and dissipation in channel flow. *J. Fluid Mech.* **996**, A12.

YU, M., CECI, A. & PIROZZOLI, S. 2022 Reynolds number effects and outer similarity of pressure fluctuations in turbulent pipe flow. *Intl J. Heat Fluid Flow* **96**, 108998.